Ultra-High Size Exclusion Selectivity for Carbon Dioxide from Nitrogen/Methane in an Ultramicroporous Metal-Organic Framework

Ellan K. Berdichevsky [a], Victoria A. Downing [a], Riley W. Hooper [b], Nathan W. Butt [a], Devon T. McGrath [a], Laurie J. Donnelly [a], Vladimir K. Michaelis [b], Michael J. Katz [a]*

[a] Department of Chemistry, Memorial University of Newfoundland, 230 Elizabeth Avenue, St. John's, Newfoundland and Labrador, A1C 5S7, Canada
E-mail: mkatz@mun.ca

[b] Department of Chemistry, University of Alberta, 11227 Saskatchewan Drive, Edmonton, Alberta, T6G 2G2, Canada

ABSTRACT: Separations based on molecular size (molecular sieving) are a solution for environmental remediation. We have synthesized and characterized two new metal-organic frameworks (**Zn$_2$M**; M = Zn, Cd) with ultramicropores (<0.7 nm) suitable for molecular sieving. We explore the synthesis of these MOFs and the role that the DMSO/H$_2$O/DMF solvent mixture has on the crystallization process. We further explore the crystallographic data for the DMSO and methanol solvated structures at 273 and 100K; this not only results in high quality structural data, but also allows us to better understand the structural features at temperatures around the gas adsorption experiments. Structurally, the main difference between the two MOFs is that the central metal in the trimetallic node can be changed from Zn to Cd and that results in a sub-Å change in the size of the pore aperture, but a stark change in the gas adsorption properties. The separation selectivity of the MOF when M = Zn is infinite given the pore aperture of the MOF can accommodate CO$_2$ while N$_2$ and/or CH$_4$ is excluded from entering the pore. Furthermore, due to the size exclusion behaviour, the MOF has an adsorption selectivity of 4800:1 CO$_2$:N$_2$ and 5×10^{28}:1 CO$_2$:CH$_4$. When M = Cd, the pore aperture of the MOF increases slightly, allowing N$_2$ and CH$_4$ to enter the pore, resulting in a 27.5:1 and a 10.5:1 adsorption selectivity, respectively; this is akin to UiO-66, a MOF that is not able to function as a molecular sieve for these gases. The data delineates how subtle sub-Å changes to the pore aperture of a framework can drastically affect both the adsorption selectivity and separation selectivity.

Introduction

Carbon dioxide, a leading greenhouse gas, requires an effective approach to separate it from other gases.[1] Conventionally, the challenge lies in the physical similarity, differences in reactivity, and/or low concentrations of constituents of the mixture.[2] For CO$_2$, this either requires efficient separation at 400 ppm from air (direct air separation/capture), at post-combustion flue gas concentrations of 10-20 vol% CO$_2$, or as high as 50% in methane-rich biogas.[3,4] Development in this area is key to addressing the efficiency and energy costs of this environmentally critical separation.[5,6] Solid adsorbents and filters have attracted considerable attention due to their tailorability to specific separations and lower regeneration costs.[5–8]

One class of adsorbent materials that has been motivated by separation/storage is metal-organic frameworks (MOFs).[7,9] Formed via the bridging of metal nodes by organic ligands (linkers), the varied 3D topologies of MOFs, and their associated pore structures, have found applications in a multitude of storage (adsorption) and separation technologies (among others).[10–16] With judicious choice of the node and linker, the pore structure, which consists of the pore aperture, pore size, and pore functionality (Figure 1), can be tuned to favorably interact with different gas molecules. For porous materials, there are three methods that can be utilized for separations, or separation and storage of materials.
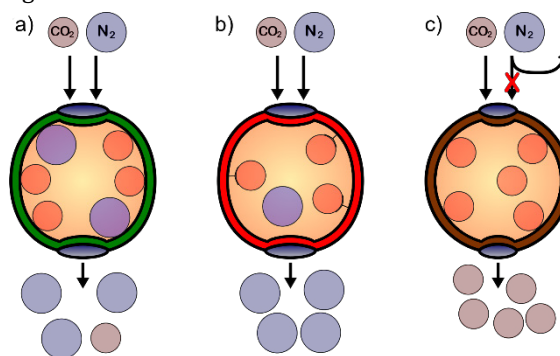

Figure 1. Modes of adsorption/separation in MOFs; a) physisorption, b) chemisorption, c) molecular sieving.

Physical adsorption (physisorption; Figure 1a) occurs when non-covalent interactions (e.g., Van der Waals) predominate. For physisorption to work efficiently, the gas of interest must have a higher enthalpy of adsorption relative to the other gases in question, and the adsorption capacity of the porous material must be sufficiently high. Under these conditions, the gas of interest is adsorbed onto the surface of the MOF. The adsorbed gas can be released, and the MOF regenerated, by heating the system or reducing the pressure (i.e., temperature-swing or pressure-swing

adsorption). Physisorption interactions are well suited to applications where regeneration and reusability of the adsorbent is important or when eventual release of the adsorbate is sought after. Physisorption has been utilized for H_2, CH_4, and CO_2 adsorption.[7,17–19]

Chemical adsorption (chemisorption; Figure 1b) relies on forming chemical bonds between the adsorbent and the adsorbate. These can be the formation of metal-ligand bonds, covalent bonding, or chemical reactivity (stoichiometric or catalytic) between the adsorbent and the adsorbate (Figure 1b). The enthalpies of adsorption for these processes are often high and not easily, if at all, reversible. Furthermore, a high degree of reactive sites is necessary to achieve a high storage/reaction capacity. To that end, chemisorption is prevalent in adsorption/separation processes where strong binding is required. These interactions have been utilized for the capture of toxic chemicals (e.g., nitrogen oxides and their precursors),[20–22] and for high specific-analyte selectivity such as CO_2.[23,24]

Table 1: Kinetic Diameters of common gases.

	Kinetic Diameter (Å)	
Gas	Breck[25]	Dal-Cin[26]
CO_2	3.3	3.42667
N_2	3.64	3.58760
CH_4	3.8	3.88178
Ar	3.4	-

The third method for the separation of gases is size dependent separation (i.e., molecular sieving) that depends on tuning the pore aperture (Figure 1c).[27] The aim of molecular sieving is to allow one species to enter the pore while others cannot. Table 1 illustrates the tight tolerance necessary to achieve molecular sieving for gas phase applications; the pore must have a pore aperture larger than the gas of interest yet smaller than the other gases in a mixture. This can lead to incredibly efficient separations. The molecular sieving approach has been demonstrated in the separation of various hydrocarbons.[28]

In the context of CO_2 separation and storage, all these methodologies have potential. However, each methodology also has limitations. One of the challenges with physisorption is that changes in temperature or partial pressure can lead to changes in the quantity adsorbed and reduce the overall adsorption, and thus separation, efficiency. For chemisorption, the high energy cost associated with adsorbent regeneration hinders its recyclability. Molecular sieving is a kinetic process. The more similar the kinetic diameters of the gases being separated, the tighter the tolerance needs to be between pore aperture and kinetic diameter of the smaller gas. This can lead to kinetic limitations (e.g., diffusion). However, sieving is uniquely suited to increase its efficiency in higher temperature applications where gases have higher kinetic energy; under these conditions, physisorption and chemisorption may suffer due to the increased thermal energy of the system.

Often, when gas separation applications are considered, then storage capacity is an important factor. This is certainly true for applications that rely on physisorption and chemisorption. However, high adsorption capacities in molecular sieves are not necessary; a mixed-matrix membrane[29] (MMM) containing a molecular sieve could be used to separate the gas of interest. The MMM could then work in tandem with a high-capacity MOF for the storage of the newly separated gas, or be coupled into reactors where CO_2 can be converted to a value added product.[30] This methodology could be used for separation and storage/utilization of CO_2 from flue gas or methane-rich biogas, and direct air capture where separation, storage, and desorption can be easily accomplished.

With the application of molecular sieving of CO_2 in mind, and our ongoing interests in chemical separations,[20,31,32] we report the synthesis and characterization of two new MOFs, $Zn_3(NH_2BDC)_3DABCO$ (**Zn₃**) and $Zn_2Cd(NH_2BDC)_3DABCO$ (**Zn₂Cd**) (NH_2BDC = 2-aminoterephthalate, DABCO = 1,4-diazabicyclo[2.2.2]octane). **Zn₃** possesses a small pore aperture that allows CO_2 to enter the pore but N_2/CH_4 cannot. This makes **Zn₃** ideal for CO_2/N_2 or CO_2/CH_4 separation while **Zn₂Cd**, with a sub-Å increase in pore aperture displays a drastic decrease in separation capability due to its ability to to allow N_2, CO_2, and CH_4 to enter and adsorb within the framework. Along with UiO-66, a prototypical MOF that contains a pore aperture that cannot be used for molecular sieving, we demonstrate the ability of **Zn₃** to act as a molecular sieve for CO_2 and the importance of optimizing molecular sieving at the sub-Å level. This demonstrates the small tolerances necessary for highly efficient molecular sieves.

Experimental

Materials and Methods

Terephthalic acid (H_2-BDC), 2-aminoterephthalic acid (H_2-NH_2BDC), 1,4-diazabicyclo[2.2.2]octane (DABCO), zinc nitrate hexahydrate ($Zn(NO_3)_2 \cdot 6H_2O$), cadmium nitrate tetrahydrate ($Cd(NO_3)_2 \cdot 4H_2O$), zirconium tetrachloride ($ZrCl_4$), hydrochloric acid (HCl), dimethylsulfoxide (DMSO), *N,N*-dimethylformamide (DMF), methanol (MeOH), methylene chloride (CH_2Cl_2), sulfuric acid (H_2SO_4), and deuterated solvents were purchased from commercial sources and used as-received.

Solution ^{1}H nuclear magnetic resonance (NMR) data were collected on a Bruker AVANCE 500 MHz spectrometer using an inverse probe. MOF samples were prepared for NMR by first digesting the crystals (5-10 mg) in H_2SO_4 (1-2 drops), then appropriate deuterated solvent was added. A water-suppression pulse program was used when collecting data.

Solid-state ^{13}C and [113]Cd NMR data were acquired on a Bruker AVANCE III HD 400 NMR spectrometer (B_0 = 9.4 T) equipped with a 4 mm double-resonance (H/X) Bruker magic-angle spinning (MAS) probe (see SI for further details). [67]Zn NMR spectra were acquired on a Bruker AVANCE II 900 NMR spectrometer (B_0 = 21.1 T). Non-spinning NMR spectra were acquired on a 7 mm home-built non-spinning probe. Spinning spectra were acquired on a 4 mm double-resonance (H/X) MAS low-γ Bruker probe (See SI for further details). All spectra were collected at natural abundance.

Powder X-ray diffraction (PXRD) patterns were collected on a Rigaku miniflex with sealed-tube X-ray source operating at 40 kV/15 mA and a D/teX Ultra detector.

Thermogravimetric analysis (TGA) was performed on a TA Instruments Q500 equipped with Thermal Advantages Software (version 5.2.6) at 10 °C/min heating rate under N_2 atmosphere.

Prior to gas adsorption measurements, all MOF samples were thermally degassed (activated) using a Micromeritics Smart VacPrep sample preparation instrument. Samples were heated (**Zn₂M** at 55 °C, UiO-66 at 150 °C) while a vacuum level below 1.00 mmHg was reached at a rate of 5.00 mmHg·s⁻¹. Then, samples were held under unrestricted vacuum for 1080 min (**Zn₂M**) or 800 min (UiO-66).

Nitrogen, argon, carbon dioxide, and methane gas adsorption isotherms were measured using a Micromeritics 3Flex Surface Characterization instrument, with the accompanying MicroActive software suite. Measurements were performed either at 77 K with liquid nitrogen, 195 K with $CO_{2(s)}$/acetone, or at/above 273 K using a VWR circulating water bath connected to an AD07R-40 temperature controller. Sample surface areas were calculated based on Brunauer-Emmett-Teller (BET) theory and associated 4-point criteria, or by Langmuir theory with associated Dual-Site Langmuir (DSL) fits (see Table S2) of CO_2 adsorption isotherms.

Pore size distributions (PSDs) were obtained using the MicroActive software suite, by examining the fits of several provided Density Functional Theory (DFT) models to the CO_2 adsorption isotherms obtained at 273 K. Goodness of the fit was evaluated based on the standard deviation of the fit from collected isotherm data, and the model with the lowest standard deviation was chosen. In all cases, this was the "GCMC CO_2 Carbon slit" model. It should be noted that the only available models were those of a slit-pore geometry, based on porous carbons, and while these models provide satisfactory fits to the collected isotherm data, they may not accurately describe the pore geometry of MOFs.

Synthesis of MOFs

UiO-66 was synthesized following previous reports.[33]

Zn₂M(NH₂BDC)₃(DABCO) (**Zn₃**, M = Zn; **Zn₂Cd**, M = Cd) was prepared by the solvothermal method. To a 25 mL Duran® glass bottle, 95 mg (0.85 mmol) of DABCO, 268 mg (1.53 mmol) H₂-NH₂BDC, and 500 mg (1.68 mmol) Zn(NO₃)₂·6H₂O (**Zn₃**), or 333 mg (1.12 mmol) Zn(NO₃)₂·6H₂O and 173 mg (0.56 mmol) Cd(NO₃)₂·4H₂O (**Zn₂Cd**) were added. The solids were dissolved with 18 mL of DMSO with the aid of sonication. Next, 1.2 mL of DMF was added, followed by 2.8 mL of deionized water, shaking in between additions. Finally, the bottle was capped and placed in a 110 °C oven for 72 h (**Zn₃**), or 48 h (**Zn₂Cd**). After the appropriate time, formation of yellow, hexagonal-shaped crystals was observed. The bottle was removed from the oven, allowed to cool, and the solution was gradually exchanged with MeOH or CH₂Cl₂ and allowed to sit for approximately 6 hours. The crystals were then washed with fresh solvent (2 × 10 mL) and left soaking (ca. 20 mL) overnight to remove any remaining DMSO (see SI for further information). The crystals were removed from the

methanol by filtration prior to any subsequent characterization. For long-term storage of the MOF, the crystals can be stored in CH₂Cl₂ for months without any noticeable change in crystallinity or gas adsorption properties. Scaleup of the reaction to 80x the procedure presented here has resulted in identical isotherms to the 1x reaction.

CAUTION: Heating DMSO has been known to cause autocatalytic decomposition and can pose a risk of explosion.[34] While we have not experienced any incidents, great care and appropriate precautions should be taken when heating DMSO to high temperatures.

Results and Discussion

Synthesis and crystal structure

Zn₃ was synthesized in a sealed glass bottle by reacting a 2:1.8:1 ratio of Zn(NO₃)₂·6H₂O:H₂-NH₂BDC:DABCO in DMSO with an additional 18.2 equivalents of DMF and 183 equivalents of water. The reaction is heated at 110 °C for 72 h; the reaction can be performed at 120 °C for 24 h, but the higher temperature often produces a small number of yellow flakes that are inconsistent with the data for **Zn₃**. Under optimal synthetic conditions, the solution NMR of the H₂SO₄-dissolved MOF (Figure S6) illustrated a 9:12 proton ratio of the aromatic protons of NH₂BDC to the DABCO protons. This indicates a 3:1 linker ratio consistent with the Zn₃(NH₂BDC)₃(DABCO) formula determined by X-ray crystallography (see below).

Returning to the synthesis of **Zn₃**, in the first 60 h of the 72 h synthesis the glass bottle shows no signs of crystal growth. However, somewhere in the subsequent 12 h surprisingly large X-ray quality crystals (>3mm in the smallest direction) appear. This suggests that rapid nucleation and subsequent crystal growth, or rapid crystal growth of existing seed crystals occurs due to some change in the solution composition. We hypothesize that this is due to the thermal degradation of DMF to formic acid (and subsequently to CO and H₂O) and dimethyl amine, which is one of the reasons that DMF is often used as the solvent in the synthesis of MOFs. In fact, if DMF is left out of the reaction, then no crystals form. That being said, we can't rule out that the thermal decomposition of DMSO to DMS is not also a contributing factor; the reaction does produce a notable odor of DMS.

To further explore the reaction conditions, we examined the role of water on the synthesis of **Zn₃**. Increasing the water content in steps of 39 equivalents demonstrated that in the absence of water or too little water (up to 78 equivalents), the reaction does not produce crystals. Further increasing the water content to 157 equivalents results in a cloudy solution with X-ray quality single crystals of **Zn₃**. At 183 equivalents, the solution was transparent and X-ray quality crystals were observed. Increasing the water content to 274 equivalents produced a cloudy solution and yellow flakes that are inconsistent with the data for **Zn₃**. The DMSO has to be kept nominally dry or the water content needs to be adjusted to account for the hygroscopic nature of the solvent; we stored our DMSO under 3 Å molecular sieves to minimize changes in water content.

The reaction to form **Zn₃** is identical in mole ratio and reagent concentration to the reaction conditions used to form

the pillared paddlewheel Zn$_2$(BDC)$_2$DABCO. The primary difference is the use of DMSO as the solvent with DMF acting as a stoichiometric reagent to react with the acid biproduct formed during MOF synthesis. The amount of DMF used in the reaction is roughly 5 equivalents for every carboxylic acid. Using no DMF or even half the amount of DMF does not produce **Zn$_3$**. The exact role of the solvent in selecting **Zn$_3$** over the pillared paddlewheel MOF, or other potential topologies, remains unclear.

Once **Zn$_3$** is formed, it can be stored in DMSO or exchanged for CH$_2$Cl$_2$ and left for months without notable change to the crystallinity. **Zn$_3$** can also be exchanged for MeOH but this often leads to a decrease in the quality of the crystals over time due to changes in the crystal size caused by a contracting of the unit cell dimensions (see crystallographic information, Table 2 and Table S6).
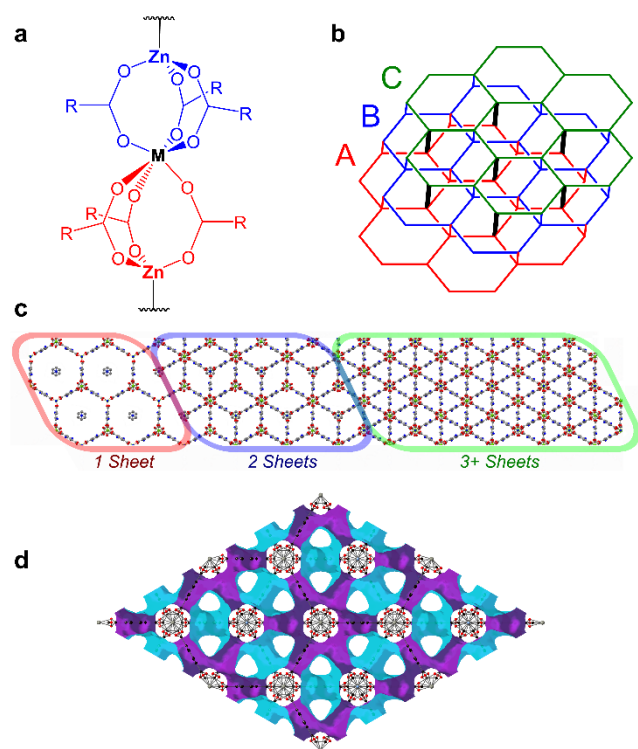

Figure 2. a) the trimetallic node of Zn$_2$M (M = Zn^{2+}, Cd^{2+}) showing an octahedral MO$_6$ unit sandwiched between two ZnO$_3$N tetrahedra (R = NH$_2$BDC). The octahedral metal acts as a fuse point for two sheets. b) an illustration showing the stacking of the individual honeycomb sheets, where bold black lines represent DABCO pillars. c) Stacking of hexagonal sheets in **Zn$_3$**, which gives the appearance of triangular shaped pores. Hydrogens and solvent molecules are omitted for clarity. Grey = C, Red = O, Blue = N, Green = Zn. See SI for larger image. d) Connolly surface with a probe size of 1.0 Å, viewed down the *c*-axis.

The crystal structure of **Zn$_3$** has been determined at both 273 and 100 K in both DMSO and MeOH-soaked samples The node of the MOF consists of three metal cations in two distinct coordination geometries: a central *fac*-ZnO$_6$ octahedron (Zn-O = 1.9236(7) Å) that is sandwiched between two ZnO$_3$N tetrahedra (Figure 2a; Zn-O = 2.1085(7) Å). Similar trimetallic nodes have been appearing more frequently in MOFs in recent years;[35–38] these trimetallic nodes have been featured in coordination polymers and

molecular compounds.[39–44] Each node contains two fused sheets, rotated 60° to one another, where each sheet forms a 2D honeycomb/hexagonal (6,3) network topology containing one tetrahedral Zn^{2+} and one of the ZnO$_6$ octahedral faces (Zn$_{1.5}$(NH$_2$BDC)$_{1.5}$; Figure 2; Figure S1). The nodes of each sheet alternate between connecting to the sheet above or to the sheet below (follow sheet B in Figure 2b, and Figure S2). The amino-units of the NH$_2$-BDC linker are not equally disordered over the 4 phenylene carbons (C(3) and C(4)) but are disordered only over C(3). This places the amino units always pointing towards the octahedral Zn (i.e., the centre of the node) rather than pointing out of the node; this may also illustrate why NH$_2$BDC is necessary and all our attempts to reproduce these structures with terephthalic acid (H$_2$-BDC) have thus far failed. The DABCO units connect every other sheet (Figure 2b; Sheet A connects to Sheet C via a DABCO unit). The overall structure can be thought of as three alternating sheets (Figure 2c). From a network topology perspective, **Zn$_3$** was evaluated as having a **bcu** topology (Figure S3).[45] Unlike a pillared paddlewheel MOF such as Zn$_2$(NH$_2$BDC)$_2$DABCO,[46] which has the same components in a different ratio and topology, the DABCO is not a structurally necessary pillar; if the DABCO could be removed or the MOF synthesized without it, then the overall structure would stay the same albeit with larger pore windows. Furthermore, unlike pillared paddlewheel MOFs, where the pillar length can be changed, due to the interconnectivity between sheets, only a pillar the length of DABCO can fit into this topology.[47]

Table 2: Unit cell parameters of Zn$_2$M in different solvents and at different temperatures.

		Zn$_3$		Zn$_2$Cd	
		a, b	*c*	*a, b*	*c*
DMSO		18.339602(17)[a]	13.981500(17)[a]	18.556000(17)[a]	14.133901(17)[a]
		18.304699(17)[b]	13.866301(14)[b]	18.526800(14)[b]	13.961600(14)[b]
MeOH		18.15761(2)[a]	13.722409(19)[a]	18.50357(2)[a]	13.96813(2)[a]
		18.12696(2)[b]	13.64843(2)[b]	18.4624(3)[b]	13.8878(3)[b]

[a] Obtained at 273 K.
[b] Obtained at 100 K.

To better understand the role that solvent has on the pore size, we examined the crystal structure of **Zn$_3$** with DMSO and MeOH soaked crystals at both 273 and 100 K. The 273K data enabled us to explore the structural features as they pertain to the gas adsorption data below. The 100 K data allowed us to better understand any changes in molecular motion in the MOF. Comparing the DMSO soaked structure, which contains a structurally resolved DMSO molecule at 273 vs. 100 K illustrates a 0.2% decrease in the *a/b* axis length with a 0.8 % decrease in the *c*-axis length; no notable structural differences were observed.

Comparing the DMSO-soaked and the MeOH-exchanged samples, we note a few key differences. In addition to the larger unit-cell (Table 2), the DMSO-containing structure crystalizes in the R -3 spacegroup with six DMSO molecules per formula unit; the DMSO units are crystallographically resolved. The MeOH-exchanged structure crystallizes in the R -3 m spacegroup with no evidence for localized molecules units; while **Zn$_3$** was exchange for MeOH, the

pore bound guest could be other guests due to the ease in which MeOH can be removed from the pore (see below). The spacegroup differences between the two samples are due to the localized DMSO units that can only be observed in three of the six sections of the hexagon-shaped pore, thereby breaking up the R -3 m symmetry. In addition to the spacegroup differences, the MeOH-exchanged structure shows whole linker disorder at 100 K for the NH₂BDC. This indicates that in the absence of a tightly filled pore (e.g., such as in DMSO), the structure is more flexible. This is further reflected in the 0.18 Å decrease in the *a/b*-axis length 0.25 Å decrease in the *c*-axis length of **Zn₃** at 273 K.

From a gas adsorption perspective, looking down the *c*-axis of the unit cell (Figure 2c; Figure S4) a guest molecule would observe a donut shaped pore with the outer edge looking like a hexagon and the donut hole being occupied by DABCO. Perpendicular to the *c*-axis there is also a smaller channel (Figure S4; Table S1). We hypothesize that the smaller channel is too small for gases to enter, and the larger channel down the *c*-axis is primarily responsible for the gas adsorption below. Based on the distances between the DABCO unit and the hexagonal wall (Figure 2c), the pore aperture appears to be on the order of the kinetic diameter of common gases (Table 1; see computational analysis below).

With the understanding of the role of the solvent in the synthesis of **Zn₃** and the structural information illustrating two different Zn geometries, we explored if the octahedral cation in the node could be exchanged. Using the same synthetic procedure, we were able to easily incorporate Cd(II) into the structure to form **Zn₂Cd**. Cd(II) is approximately 13% larger than Zn(II) and readily adopts an octahedral geometry. As such, it presents the most obvious metal substitution. **Zn₂Cd** is isostructural to **Zn₃**. Crystallographically, only the central metal in the node appears to have been exchanged. Even reactions where a 1:2 ratio of Zn:Cd is attempted results in a 2:1 ratio in the structure. Structurally, the main difference between **Zn₃** and **Zn₂Cd** is that the unit cell is 1.2 % larger in the *a/b*-axis and 0.7% larger along the *c*-axis at 100 K for the DMSO-containing structure (Table 2; Table S7); this change is due to the larger atom as evident by the longer Cd-O octahedral bond lengths and unchanged, relative to **Zn₃**, Zn-O tetrahedral bond lengths. This slight change increases the size of the pore aperture for **Zn₂Cd** over **Zn₃** (see below). Additionally, the NH₂BDC linker disorder in **Zn₂Cd** indicates more libation about the linker's molecular *z*-axis.

With the mind set of gas adsorption, we further explored the role of the DMSO/MeOH on the structural parameters. As shown in Table 2, going from 273 to 100 K showed a similar absolute change in the unit cell dimensions from **Zn₃** to **Zn₂Cd**. However, there is a much larger decrease in the axis lengths when DMSO is exchanged for MeOH in **Zn₃** than in **Zn₂Cd**. This suggest that the DMSO is more constrained in **Zn₃** and the structure shrinks once the DMSO is exchanged. This suggests that when a pore-bound guest is almost too big to fit in the structure, the structure can stretch to some degree to allow for it to incorporate the guest (see gas adsorption below).

To further explore the structure of these materials, we examined the powder X-ray diffraction patterns of **Zn₃** and

Zn₂Cd. Figure 3 shows the simulated PXRD for the DMSO-containing and MeOH-exchanged samples as well as the observed diffraction patterns for the DMSO-containing and MeOH-exchanged **Zn₃** and **Zn₂Cd**. Crystals of both MOFs grow as large hexagons along the *c*-axis that results in preferred orientation; this can be best seen by comparing the {1 0 1} reflection (the first reflection) vs. the {2 -1 0} reflection just shy of 10 °. Of particular note is the effect of solvent on the diffraction pattern. The smaller pore sizes of these MOFs lead to more localized solvents that lead to more pronounced differences in the diffraction pattern; this is especially observed in the DMSO-containing structures where the intensity differences between the observed and measured diffractograms are more pronounced. For the MeOH-exchanged samples, where the solvent in the pore is more dynamic, the observed and calculated diffraction patterns are more similar. Overall, the diffraction patterns of these samples coupled with the single crystal X-ray diffraction indicate that solvent exchange of the MOF does not lead to a change in the topology.
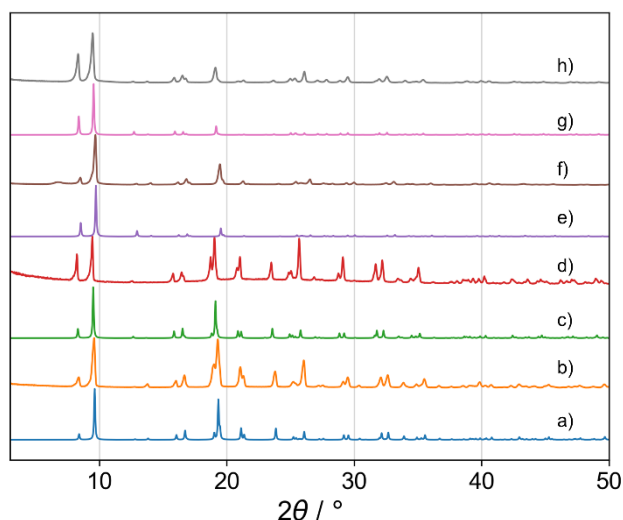

Figure 3. PXRD diffractograms of a) Simulated **Zn₃** with pore-occupying DMSO, b) **Zn₃** as synthesized from DMSO, c) Simulated **Zn₂Cd** with pore-occupying DMSO, d) **Zn₂Cd** as synthesized from DMSO, e) Simulated **Zn₃**, methanol exchanged (no crystallographically-defined solvent in the pore), f) **Zn₃** after methanol exchange, g) Simulated **Zn₂Cd**, methanol exchanged (no crystallographically defined solvent in the pore), h) **Zn₂Cd** after methanol exchange.

Once the solvent was removed from the MOFs (i.e., activation), significant peak broadening was observed (Figure S5). This is indicative of the highly flexible nature of these frameworks, as we noted from single crystal data. Re-solvation of **Zn₃** (i.e., refilling the framework with solvent) could be accomplished by stirring the MOF in DMF over several hours, and the PXRD pattern again looks like the solvent-exchanged form. In the case of **Zn₂Cd**, while peak broadening did occur, it was not to the same extent as what we observed with **Zn₃**. This is consistent with the comparatively smaller changes to the unit cell of **Zn₂Cd** upon solvent exchange (Table 2). As a result, no noticeable change was observed in the diffraction pattern after suspension of the MOF in DMF.
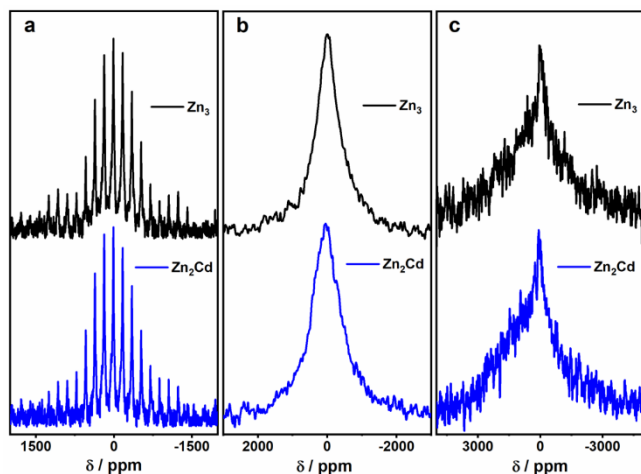
Solid-State NMR investigation

Figure 4. Solid-state ^{67}Zn NMR spectra for **Zn₃** and **Zn₂Cd** (B₀ = 21.1 T). From L to R: CPMG (**a**) and quad-echo under non-spinning (**b**) and MAS (**c**, ν_{rot} = 15 kHz) conditions.

To compliment the average long-range structure from diffraction, the local chemical environments of the trimetallic node was studied using solid-state NMR spectroscopy. Solid-state ^{67}Zn NMR has had some success in microporous materials.[48–50] Figure 4 displays the solid-state ^{67}Zn NMR spectra at natural abundance, revealing broad unresolved resonances with peak maxima at -22 (**Zn₃**) and 34 (**Zn₂Cd**) ppm. The distinction between the samples is seen from the linewidth, whereby a FWHM of 47 kHz is observed for **Zn₃** while the Cd incorporation increases this to 55 kHz (**Zn₂Cd**). The broadening observed in **Zn₂Cd** suggests a change in the medium-range structure of the tetrahedral Zn sites when Cd replaces the Zn octahedral fuse point within these isostructural MOFs. A distortion of the electric field gradient and local disorder can be envisioned when the smaller Zn^{2+} is replaced by the larger isoelectronic Cd^{2+} that induces strain on the ZnO_3N pocket (Zn-O bond lengths are greater in **Zn₂Cd**) above and below the Cd plane. ^{13}C NMR (Figure S11) further supports this finding where the **Zn₃** spectrum is much better resolved than its **Zn₂Cd** counterpart. This indicates that **Zn₃** is locally ordered, while **Zn₂Cd** is disordered due to increased flexibility within the framework with the introduction of the Cd^{2+} ion. Unfortunately, due to the limited sensitivity of ^{67}Zn NMR (short spin-spin relaxation, quadrupolar nature (I=5/2) and low natural abundance) we are precluded from obtaining higher resolution data and turn our attention to ^{113}Cd NMR that is ~12-fold more sensitive. The ^{113}Cd NMR spectrum of **Zn₂Cd** (Figure S12) reveals a single Cd resonance with an δ_{iso}= -36 ppm and a FWHM = 3.3 kHz. The chemical shift and absence of magnetic shielding anisotropy is consistent with a highly symmetric six-coordinate $[CdO_6]$ chemical environment (i.e., the observed *fac*-MO_6 symmetry).[51] No evidence of a secondary site is seen, supporting isolated d^{10} Zn/Cd substitution only in the octahedral site.

Computational Pore Analysis

To determine the pore characteristics of the MOF, we calculated the pore aperture as well as the pore width of both **Zn₃** and **Zn₂Cd** using the PoreBlazer software package (Table 3).[52]

For **Zn₃**, in the DMSO-solvated structure, 44% of the structure is empty with a pore aperture of 3.47 Å and a pore width of 4.90 Å (Figure 2d). When the DMSO is exchanged for MeOH, the pore aperture of **Zn₃** decreases to 3.29 Å, with a concomitant decrease in pore width to 4.80 Å. Given the larger size of the unit cell of **Zn₂Cd** relative to **Zn₃** (Table 2), it is not surprising that the DMSO-containing structure of **Zn₂Cd** has a larger pore aperture and pore width of 4.08 Å and 5.03 Å, respectively. After MeOH exchange, the pore aperture and width decrease to 3.09 Å and 5.05 Å, respectively. The smaller value obtained for the pore aperture of **Zn₂Cd** relative to **Zn₃** in the MeOH-exchanged samples is almost certainly due to the crystallographic disorder of the NH₂BDC linkers. Given that the pore widths of **Zn₂Cd** are not considerably different after solvent exchange, the actual pore aperture is likely also unchanged

For both **Zn₃** and **Zn₂Cd**, factoring in that the disorder of the MeOH-exchanged structures leads to an underestimation of the pore sizes, the pore apertures of these MOFs (Figure S3 and Table S1) are approximately the size of the kinetic diameters of small gas molecules such as CH_4, N_2, CO_2, or similar gases. This indicates that these materials, **Zn₃** in particular, may be ideal for molecular sieving applications.

Table 3. Pore dimensions of Zn₂M calculated with PoreBlazer from crystal structures obtained at 273 K.

	Zn₃		Zn₂Cd	
	Aperture (Å)	Width (Å)	Aperture (Å)	Width (Å)
DMSO	3.47	4.90	4.08	5.03
MeOH	3.29	4.80	3.09	5.05

Gas Adsorption Analysis

In preparation for gas adsorption studies, **Zn₃** and **Zn₂Cd** were first solvent exchanged in MeOH overnight. With these narrow aperture MOFs, we examined the efficacy of solvent exchange by NMR and TGA. We looked at time-resolved solution NMR of a sealed NMR tube containing crystals of **Zn₃** in methanol-d_3. As shown in Figure S7, the amount of DMSO leaching into solution from the crystals ceased after 18 h. Dissolution of crystals of **Zn₃** and **Zn₂Cd** in H_2SO_4/CD_3OD after soaking (Figure S8 and S9 respectively) showed no evidence of DMSO remaining in the crystals. To further explore this, we examined the TGA of **Zn₃** and **Zn₂Cd** (Figure S10). The as-synthesized MOFs show that the decomposition temperature of the MOF and the removal of DMSO occur at too similar a temperature range for successful activation of the material. However, upon successful solvent exchange with methanol, both MOFs can be activated at 55 °C for gas adsorption studies.
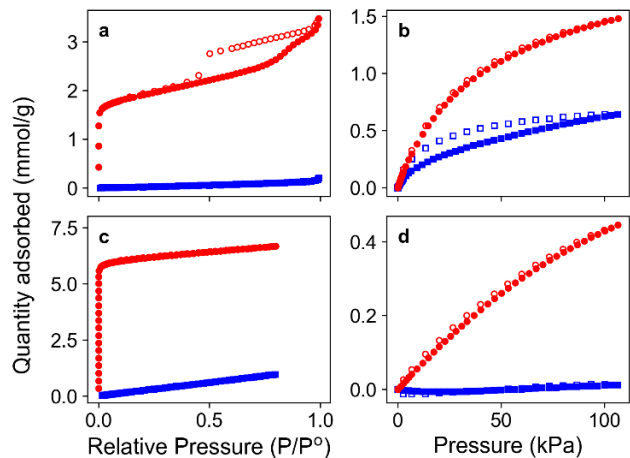
Figure 5. Gas adsorption isotherms for **Zn₃** (blue squares) and **Zn₂Cd** (red circles): a) N_2 at 77 K. b) CO_2 at 273 K. c) Ar at 77 K. d) CH_4 at 273 K. Adsorption and desorption are represented with filled and empty symbols, respectively.

To assess the pore aperture of **Zn₃** and **Zn₂Cd**, we examined the gas adsorption properties of these MOFs for CO_2, Ar, N_2, and CH_4; these gases have ever-increasing kinetic diameters (Table 1). All the data shown in Figure 5 is reproducible within reasonable errors (see Figures S13-S22 for additional isotherms). For **Zn₂Cd** all four gas molecules are able to enter the pore of the MOF; this aligns well with the computational data, and puts a lower-limit for the pore aperture at 3.8 Å. The N_2-accessible surface area of **Zn₂Cd**, determined at 77 K is 140 m^2/g (Table 4). This is corroborated from the dual site Langmuir fits of the CO_2 isotherms (Table 4; 150 m^2/g).

For **Zn₃**, only CO_2 enters the pore of the MOF. The surface area of **Zn₃** is calculated to be between 85 and 100 m^2/g (Table 4). This suggests that **Zn₃** has a pore aperture that is smaller than N_2 but larger than CO_2 (Table 1) and is thus able to separate gases with kinetic diameters between this range. This is consistent with the computational data shown in Table 3. **Zn₃**, while not best suited for the storage of CO_2, is capable of sieving CO_2 from N_2/CH_4 gas with a theoretically infinite separation selectivity and could more effectively be used in an MMM system.

Comparing the CO_2 isotherms of **Zn₃** and **Zn₂Cd** (Figure 5b), we note that **Zn₃** shows hysteresis. We propose that the CO_2-filled pores result in a rigidification of the previously flexible, unoccupied structure. Thus, desorption of the tightly bound CO_2 becomes more challenging. This effect can be seen in the lack of disorder in the DMSO vs. MeOH solvated structures as well as the unit cell difference between these structures (Table 2). This is not observed for **Zn₂Cd** where these confinement effects are no longer possible due to the sub-Å increase in pore properties.

To further explore the potential confinement effects in **Zn₃**, we examined the enthalpies (heats) of adsorption (Q_{st}). For **Zn₃**, dual-site Langmuir models, using the method by Long and co-workers,[53] were necessary to get good fits. As shown in Figure 6 (Figures S25, S26, and Tables S2, S3), the Q_{st} for **Zn₃** are relatively high (40.2 kJ/mol at zero loading)[54] up until 50% of the total storage capacity of **Zn₃** (Table S2; ~0.4 CO_2/Zn₃ formula unit or 0.5 mmol/g). Afterwards, the CO_2 adsorption energy is 15 kJ/mol, consistent

with the heat of vaporization for CO_2 (16.7 kJ/mol). Simply opening the pore dimensions to **Zn₂Cd**, the fits showed only sight deviations from single-site Langmuir isotherms with a slight decrease in Q_{st} value over the adsorption range; the data look remarkably like a traditional MOF (UiO-66; Figure S26).[55] The higher enthalpies and strongly varying Q_{st} values as a function of loading confirm the confinement effects in **Zn₃**.[56] If this was simply due to the amine functionality of the linker, which has been demonstrated by others,[55,57,58] then we would expect both **Zn₃** and **Zn₂Cd** to show high enthalpies of adsorption.
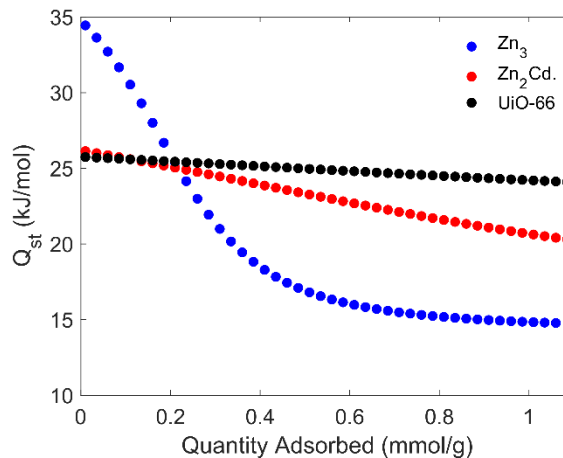

Figure 6. Isosteric heats of adsorption (Q_{st}) of CO_2, calculated at 290 K.

Table 4. Measured gas uptake (mmol/g) at different temperatures and corresponding surfaces areas (SA, m^2/g).

Sample	SA (m^2/g)	CO_2 (mmol/g)				CH_4 (mmol/g)
		273 K	285 K	290 K	295 K	273 K
Zn₃	100,[a] 85[b]	0.64	0.45	0.42	0.40	-
Zn₂Cd	150,[a] 140[c]	1.48	0.94	0.90	0.83	0.43
UiO-66	1560[c]	2.55	2.04	1.84	1.64	0.61

[a] Surface area from Dual-Site Langmuir fit of CO_2 isotherms.
[b] Brunauer-Emmett-Teller (BET) surface area from CO_2 gas adsorption (195 K).
[c] BET surface area from N_2 gas adsorption (77 K).

To compare **Zn₃** to other molecular sieves, we calculated the CO_2/N_2 and CO_2/CH_4 adsorption selectivity (S_{CO_2/N_2}, and S_{CO_2/CH_4}, respectively) from single-component adsorption isotherms using Ideal Adsorbed Solution Theory (IAST).[59] As IAST relies on both gases being able to adsorb, the selectivity values obtained for molecular sieves are often highly dependent on instrumental uncertainties. Nonetheless, selectivities calculated using IAST are still often used as a form of qualitative comparison between materials. The IAST++ software suite[60] was used to simulate mixed-gas adsorption isotherms from fits of the single-component isotherms in order to calculate the appropriate selectivity. As shown in Figure 7 and Figures S29, at post-combustion flue gas concentration (15:85 CO_2/N_2), **Zn₃** possess a very large S_{CO_2/N_2} (4800 at 100 kPa and 295 K).

Likewise, an adsorption selectivity of $\sim10^{28}$ at 100 kPa and 273 K for S_{CO_2/CH_4} (50:50 CO_2/CH_4, Figure S29, Table S5). This places **Zn₃** among the best molecular sieves for CO_2 (Table S4).[3,61–63] We should be diligent when presented with such large selectivity values, as it also follows that N_2 and CH_4 inaccessible MOFs should approach infinite adsorption selectivity for CO_2 as pressure increases, barring gating effects,[64] and the value obtained will be affected by the uncertainties of the N_2 and CH_4 isotherm measurement.[9] These results nonetheless illustrate the sieving behaviour of **Zn₃**.
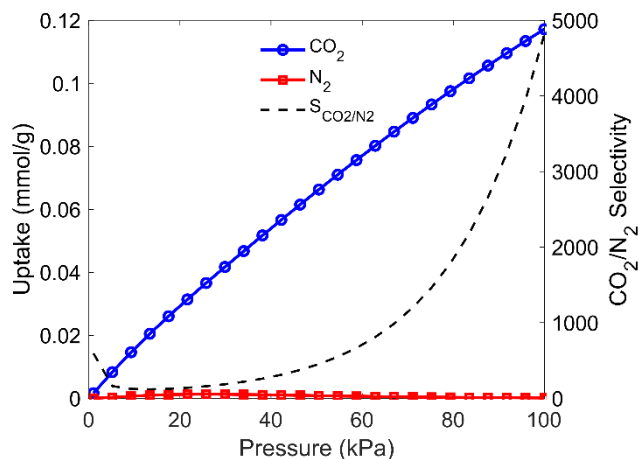
Figure 7. IAST selectivity and simulated uptake of 15:85 CO_2/N_2 binary mixture of **Zn₃** at 295 K.

In contrast to **Zn₃**, **Zn₂Cd** has a S_{CO_2/N_2} of 31-27.5 and a S_{CO_2/CH_4} of 8.8-10.5 from 0-100 kPa (Figures S27, S30) demonstrating the remarkable effect that sub-Å pore aperture tailoring has on selectivity. The increase observed in S_{CO_2/CH_4} for **Zn₂Cd** may suggest improvement of separation selectivity as pressure increases. Further study in a high-pressure system is required to confirm this. To further illustrate how the sub-Å changes in pore sizes affect selectivity, we repeated the IAST calculations for UiO-66. As shown in Figures S28 and S31, UiO-66 has a S_{CO_2/N_2} of 19.5-18 and a S_{CO_2/CH_4} of 15-8.5 from 0-100 kPa. This demonstrates how a sub-Å change in the pore aperture from **Zn₃** to **Zn₂Cd** can make an ultramicroporous (**Zn₂Cd**) MOF behave like a traditional porous MOF (UiO-66) in the context of separation efficiency.

Conclusion

In summary, two *de novo* and isostructural ultramicroporous MOFs were synthesized and characterized. For **Zn₃** we demonstrate that the MOF is porous the CO_2 but larger gases such as N_2 or CH_4, are too large to enter the pore and are thus in accessible to the pore surface. Remarkably, a subtle change in pore aperture that would be unimportant in many large pore MOFs leads to a drastic change in separation selectivity. The sub-Å aperture tuning presented here from going from **Zn₃** to **Zn₂Cd**, enabled by modifying a multi-nuclear node, can lead to other attractive separations such as acetylene/ethene, noble gas purification, or helium recycling, where small precisely-sized apertures would offer an energy-efficient alternative to current technologies.

The challenge we now face is the implementation of such molecular sieving MOFs. The low adsorption capacity of **Zn₃** and **Zn₂Cd** make these MOFs ideal for separations where efficacy is critical and where storage or isosteric heats are not a metric for the success of a material. These applications range from higher temperature applications and applications where the gas of interest exists at a low partial pressure where adsorption is inefficient. We envision the use of **Zn₃**, with its remarkable sieving capabilities, in a pristine MOF-incorporated membrane where it can be utilized in applications where pressure differentials are more meaningful than adsorption capacity. Such membranes may show promise in carbon separation processes, such as direct air capture where most MOFs struggle to adsorb at 400 ppm, coupled with oxy-fuel combustion, or bioenergy production, where the separated CO_2 can be directly reintroduced into the process rather than needing to be stored in the adsorbent.[4] Furthermore, coupling these membranes with a high adsorption capacity but low selectivity MOF would show interesting promise in for various carbon capture applications.

Currently, we are studying the properties of these MOFs via breakthrough experiments in MMMs and fixed bed adsorption. For microporous MOFs such as these, performing such experiments is non-trivial and requires careful considerations to tease out the efficacy of the MOF vs. the flow rate of the gases (i.e., kinetics of gas transport through a porous network).

ASSOCIATED CONTENT

AUTHOR INFORMATION

Corresponding Author
* mkatz@mun.ca
Notes
The authors declare no competing financial interest.

ACKNOWLEDGMENT

REFERENCES

(1) Aaron, D.; Tsouris, C. Separation of CO_2 from Flue Gas: A Review. *Sep. Sci. Technol.* **2005**, *40*, 321–348, DOI: 10.1081/SS-200042244.

(2) Sholl, D. S.; Lively, R. P. Seven Chemical Separations to Change the World. *Nature* **2016**, *532*, 435–437, DOI: 10.1038/532435a.

(3) Wang, Y.; Zhao, D. Beyond Equilibrium: Metal–Organic Frameworks for Molecular Sieving and Kinetic Gas Separation. *Cryst. Growth Des.* **2017**, *17*, 2291–2308, DOI: 10.1021/acs.cgd.7b00287.

(4) Siegelman, R. L.; Kim, E. J.; Long, J. R. Porous Materials for Carbon Dioxide Separations. *Nat. Mater.* **2021**, *20*, 1060–1072, DOI: 10.1038/s41563-021-01054-8.

(5) Ma, Y.; Zhang, F.; Lively, R. P. Manufacturing Nanoporous Materials for Energy-Efficient Separations. In *Sustainable Nanoscale Engineering*; Elsevier, 2020; pp 33–81.

(6) Kang, Z.; Fan, L.; Sun, D. Recent Advances and Challenges of Metal–Organic Framework Membranes for Gas Separation. *J. Mater. Chem. A* **2017**, *5*, 10073–10091, DOI: 10.1039/C7TA01142C.

(7) Li, H.; Li, L.; Lin, R.-B.; Zhou, W.; Zhang, Z.; Xiang, S.; Chen, B. Porous Metal-Organic Frameworks for Gas Storage and Separation: Status and Challenges. *EnergyChem* **2019**, *1*, 100006, DOI: 10.1016/j.enchem.2019.100006.

(8) Samanta, A.; Zhao, A.; Shimizu, G. K. H.; Sarkar, P.; Gupta, R. Post-Combustion CO_2 Capture Using Solid Sorbents: A Review. *Ind. Eng. Chem. Res.* **2012**, *51*, 1438–1463, DOI: 10.1021/ie200686q.

(9) Adil, K.; Belmabkhout, Y.; Pillai, R. S.; Cadiau, A.; Bhatt, P. M.; Assen, A. H.; Maurin, G.; Eddaoudi, M. Gas/Vapour Separation Using Ultra-Microporous Metal-Organic Frameworks: Insights into the Structure/Separation Relationship. *Chem. Soc. Rev.* **2017**, *46*, 3402–3430, DOI: 10.1039/c7cs00153c.

(10) Zhang, X.; Wasson, M. C.; Shayan, M.; Berdichevsky, E. K.; Ricardo-Noordberg, J.; Singh, Z.; Papazyan, E. K.; Castro, A. J.; Marino, P.; Ajoyan, Z.; Chen, Z.; Islamoglu, T.; Howarth, A. J.; Liu, Y.; Majewski, M. B.; Katz, M. J.; Mondloch, J. E.; Farha, O. K. A Historical Perspective on Porphyrin-Based Metal–Organic Frameworks and Their Applications. *Coord. Chem. Rev.* **2021**, *429*, 213615, DOI: 10.1016/j.ccr.2020.213615.

(11) Lu, W.; Wei, Z.; Gu, Z.-Y.; Liu, T.-F.; Park, J.; Park, J.; Tian, J.; Zhang, M.; Zhang, Q.; Gentle III, T.; Bosch, M.; Zhou, H.-C. Tuning the Structure and Function of Metal–Organic Frameworks via Linker Design. *Chem. Soc. Rev.* **2014**, *43*, 5561–5593, DOI: 10.1039/C4CS00003J.

(12) Farha, O. K.; Yazaydin, A. Ö.; Eryazici, I.; Malliakas, C. D.; Hauser, B. G.; Kanatzidis, M. G.; Nguyen, S. T.; Snurr, R. Q.; Hupp, J. T. De Novo Synthesis of a Metal-Organic Framework Material Featuring Ultrahigh Surface Area and Gas Storage Capacities. *Nat. Chem.* **2010**, *2*, 944–948, DOI: 10.1038/nchem.834.

(13) Smith, M. K.; Mirica, K. A. Self-Organized Frameworks on Textiles (SOFT): Conductive Fabrics for Simultaneous Sensing, Capture, and Filtration of Gases. *J. Am. Chem. Soc.* **2017**, *139*, 16759–16767, DOI: 10.1021/jacs.7b08840.

(14) Dolgopolova, E. A.; Rice, A. M.; Martin, C. R.; Shustova, N. B. Photochemistry and Photophysics of MOFs: Steps towards MOF-Based Sensing Enhancements. *Chem. Soc. Rev.* **2018**, *47*, 4710–4728, DOI: 10.1039/c7cs00861a.

(15) García-García, P.; Müller, M.; Corma, A. MOF Catalysis in Relation to Their Homogeneous Counterparts and Conventional Solid Catalysts. *Chem. Sci.* **2014**, *5*, 2979–3007, DOI: 10.1039/c4sc00265b.

(16) Alqadami, A. A.; Naushad, M.; Alothman, Z. A.; Ghfar, A. A. Novel Metal-Organic Framework (MOF) Based Composite Material for the Sequestration of U(VI) and Th(IV) Metal Ions from Aqueous Environment. *ACS Appl. Mater. Inter.* **2017**, *9*, 36026–36037, DOI: 10.1021/acsami.7b10768.

(17) Li, Y.; Yang, R. T. Gas Adsorption and Storage in Metal–Organic Framework MOF-177. *Langmuir* **2007**, *23*, 12937–12944, DOI: 10.1021/la702466d.

(18) Wang, S.; Belmabkhout, Y.; Cairns, A. J.; Li, G.; Huo, Q.; Liu, Y.; Eddaoudi, M. Tuning Gas Adsorption Properties of Zeolite-like Supramolecular Assemblies with gis Topology via Functionalization of Isoreticular Metal-Organic Squares. *ACS Appl. Mater. Inter.* **2017**, *9*, 33521–33527, DOI: 10.1021/acsami.7b06010.

(19) Kivi, C. E.; Gelfand, B. S.; Dureckova, H.; Ho, H. T. K.; Ma, C.; Shimizu, G. K. H.; Woo, T. K.; Song, D. 3D Porous Metal–Organic Framework for Selective Adsorption of Methane over Dinitrogen under Ambient Pressure. *Chem. Commun.* **2018**, *54*, 14104–14107, DOI: 10.1039/C8CC07756H.

(20) McGrath, D. T.; Ryan, M. D.; Macinnis, J. J.; Vandenboer, T. C.; Young, C. J.; Katz, M. J. Selective Decontamination of the Reactive Air Pollutant Nitrous Acid: Via Node-Linker Cooperativity in a Metal-Organic Framework. *Chem. Sci.* **2019**, *10*, 5576–5581, DOI: 10.1039/c9sc01357a.

(21) Allan, P. K.; Wheatley, P. S.; Aldous, D.; Mohideen, M. I.; Tang, C.; Hriljac, J. A.; Megson, I. L.; Chapman, K. W.; De Weireld, G.; Vaesen, S.; Morris, R. E. Metal–Organic Frameworks for the Storage and Delivery of Biologically Active Hydrogen Sulfide. *Dalton Trans.* **2012**, *41*, 4060, DOI: 10.1039/c2dt12069k.

(22) Ingleson, M. J.; Heck, R.; Gould, J. A.; Rosseinsky, M. J. Nitric Oxide Chemisorption in a Postsynthetically Modified Metal–Organic Framework. *Inorg. Chem.* **2009**, *48*, 9986–9988, DOI: 10.1021/ic9015977.

(23) Martínez, F.; Sanz, R.; Orcajo, G.; Briones, D.; Yángüez, V. Amino-Impregnated MOF Materials for CO_2 Capture at Post-Combustion Conditions. *Chem. Eng. Sci.* **2016**, *142*, 55–61, DOI: 10.1016/j.ces.2015.11.033.

(24) Demessence, A.; D'Alessandro, D. M.; Foo, M. L.; Long, J. R. Strong CO_2 Binding in a Water-Stable, Triazolate-Bridged Metal–Organic Framework Functionalized with Ethylenediamine. *J. Am. Chem. Soc.* **2009**, *131*, 8784–8786, DOI: 10.1021/ja903411w.

(25) Breck, D. W. *Zeolite Molecular Sieves : Structure, Chemistry, and Use* ; Wiley: New York, 1973.

(26) Dal-Cin, M. M.; Kumar, A.; Layton, L. Revisiting the Experimental and Theoretical Upper Bounds of Light Pure Gas Selectivity-Permeability for Polymeric Membranes. *J. Memb. Sci.* **2008**, *323*, 299–308, DOI: 10.1016/j.memsci.2008.06.027.

(27) Nugent, P.; Belmabkhout, Y.; Burd, S. D.; Cairns, A. J.; Luebke, R.; Forrest, K.; Pham, T.; Ma, S.; Space, B.; Wojtas, L.; Eddaoudi, M.; Zaworotko, M. J. Porous Materials with Optimal Adsorption Thermodynamics and Kinetics for CO_2 Separation. *Nature* **2013**, *495*, 80–84, DOI: 10.1038/nature11893.

(28) Cui, W. G.; Hu, T. L.; Bu, X. H. Metal–Organic Framework Materials for the Separation and Purification of Light Hydrocarbons. *Adv. Mater.* **2020**, *32*, DOI: 10.1002/adma.201806445.

(29) Kalaj, M.; Bentz, K. C.; Ayala, S.; Palomba, J. M.; Barcus, K. S.; Katayama, Y.; Cohen, S. M. MOF-Polymer Hybrid Materials: From Simple Composites to Tailored Architectures. *Chem. Rev.* **2020**, *120*, 8267–8302, DOI: 10.1021/acs.chemrev.9b00575.

(30) Ding, M.; Flaig, R. W.; Jiang, H. L.; Yaghi, O. M. Carbon Capture and Conversion Using Metal-Organic Frameworks and MOF-Based Materials. *Chem. Soc. Rev.* **2019**, *48*, 2783–2828, DOI: 10.1039/c8cs00829a.

(31) Furlong, B. J.; Katz, M. J. Bistable Dithienylethene-Based Metal-Organic Framework Illustrating Optically Induced Changes in Chemical Separations. *J. Am. Chem. Soc.* **2017**, *139*, 13280–13283, DOI: 10.1021/jacs.7b07856.

(32) Zhang, J.; DeCoste, J. B.; Katz, M. J. Investigating the Cheletropic Reaction between Sulfur Dioxide and Butadiene-Containing Linkers in UiO-66. *Can. J. Chem.* **2018**, *96*, 139–143, DOI: 10.1139/cjc-2017-0306.

(33) Katz, M. J.; Brown, Z. J.; Colón, Y. J.; Siu, P. W.; Scheidt, K. A.; Snurr, R. Q.; Hupp, J. T.; Farha, O. K. A Facile Synthesis of UiO-66, UiO-67 and Their Derivatives. *Chem. Commun.* **2013**, *49*,

9449–9451, DOI: 10.1039/c3cc46105j.

(34) Deguchi, Y.; Kono, M.; Koizumi, Y.; Izato, Y. I.; Miyake, A. Study on Autocatalytic Decomposition of Dimethyl Sulfoxide (DMSO). *Org. Process Res. Dev.* **2020**, DOI: 10.1021/acs.oprd.0c00113.

(35) Hawxwell, S. M.; Adams, H.; Brammer, L. Two-Dimensional Metal-Organic Frameworks Containing Linear Dicarboxylates. *Acta Crystallogr. B* **2006**, *62*, 808–814, DOI: 10.1107/S0108768106033283.

(36) Liu, Y. L.; Yue, K. F.; Shan, B. H.; Xu, L. L.; Wang, C. J.; Wang, Y. Y. A New 3-Fold Interpenetrated Metal-Organic Framework (MOF) Based on Trinuclear Zinc(II) Clusters as Secondary Building Unit (SBU). *Inorg. Chem. Commun.* **2012**, *17*, 30–33, DOI: 10.1016/j.inoche.2011.12.008.

(37) Semitut, E. Y.; Sukhikh, T. S.; Filatov, E. Y.; Anosova, G. A.; Ryadun, A. A.; Kovalenko, K. A.; Potapov, A. S. Synthesis, Crystal Structure, and Luminescent Properties of Novel Zinc Metal-Organic Frameworks Based on 1,3-bis(1,2,4-triazol-1-yl)propane. *Cryst. Growth Des.* **2017**, *17*, 5559–5567, DOI: 10.1021/acs.cgd.7b01133.

(38) Wu, D.; Zhou, K.; Tian, J.; Liu, C.; Tian, J.; Jiang, F.; Yuan, D.; Zhang, J.; Chen, Q.; Hong, M. Induction of Chirality in a Metal–Organic Framework Built from Achiral Precursors. *Angew. Chem. Int. Ed.* **2021**, *60*, 3087–3094, DOI: 10.1002/anie.202013885.

(39) Gavrilenko, K. S.; Punin, S. V.; Cador, O.; Golhen, S.; Ouahab, L.; Pavlishchuk, V. V. In Situ Generation of Carboxylate: An Efficient Strategy for a One-Pot Synthesis of Homo- and Heterometallic Polynuclear Complexes. *J. Am. Chem. Soc.* **2005**, *127*, 12246–12253, DOI: 10.1021/ja050451p.

(40) Gavrilenko, K. S.; Gal, Y. Le; Cador, O.; Golhen, S.; Ouahab, L. First Trinuclear Paramagnetic Transition Metal Complexes with Redox Active Ligands Derived from TTF: $Co_2M(PhCOO)_6(TTF-CH-CH-Py)_2 \cdot 2CH_3CN$, M = Co^{II}, Mn^{II}. *Chem. Commun.* **2007**, No. 3, 280–282, DOI: 10.1039/B613191C.

(41) Gogoleva, N. V.; Shmelev, M. A.; Kiskin, M. A.; Aleksandrov, G. G.; Sidorov, A. A.; Eremenko, I. L. Influence of Geometric and Electronic Features of Pyridine Derivatives and Triethylamine on the Formation of a Metal Carboxylate Core in Reactions Producing Cadmium(II) Pivalate Complexes. *Russ. Chem. Bull.* **2016**, *65*, 1198–1207, DOI: 10.1007/s11172-016-1436-6.

(42) Kim, J.; Jo, H.; Yoon, S. W.; Lee, M. H.; Choi, W.; Choi, K.; Ok, K. M. Synthesis, Structure, and Characterization of Variable Chains in a Series of Transition Metal Coordination Compounds. *Eur. J. Inorg. Chem.* **2020**, *2020*, 452–460, DOI: 10.1002/ejic.201901188.

(43) Li, X.; Ma, D.; Cao, B.; Lu, Y. Windmill-Type Mixed-Metal Clusters Containing Schiff-Base Ligands as an Efficient Catalyst for Cyclohexene Oxidation. *New J. Chem.* **2017**, *41*, 11619–11625, DOI: 10.1039/C7NJ02359F.

(44) Wang, C.-F.; Zhu, Z.-Y.; Zhang, Z.-X.; Chen, Z.-X.; Zhou, X.-G. Crystal Engineering of Zinc(II) and Copper(II) Complexes Containing 3,5-dimethylisoxazole-4-carboxylate Ligand via O–H···N, C–H···A (A = N, O and π) and Bifurcated C–H···N/O Interactions. *CrystEngComm* **2007**, *9*, 35–38, DOI: 10.1039/B615091H.

(45) O'Keeffe, M.; Peskov, M. A.; Ramsden, S. J.; Yaghi, O. M. The Reticular Chemistry Structure Resource (RCSR) Database of, and Symbols for, Crystal Nets. *Acc. Chem. Res.* **2008**, *41*, 1782–1789, DOI: 10.1021/ar800124u.

(46) McGrath, D. T.; Downing, V. A.; Katz, M. J. Investigating the Crystal Engineering of the Pillared Paddlewheel Metal–Organic Framework $Zn_2(NH_2BDC)_2DABCO$. *CrystEngComm* **2018**, *20*, 6082–6087, DOI: 10.1039/C8CE00848E.

(47) Zhang, Z.; Nguyen, H. T. H.; Miller, S. A.; Ploskonka, A. M.; Decoste, J. B.; Cohen, S. M. Polymer-Metal-Organic Frameworks (PolyMOFs) as Water Tolerant Materials for Selective Carbon Dioxide Separations. *J. Am. Chem. Soc.* **2016**, *138*, 920–925, DOI: 10.1021/jacs.5b11034.

(48) Sutrisno, A.; Terskikh, V. V.; Shi, Q.; Song, Z.; Dong, J.; Ding, S. Y.; Wang, W.; Provost, B. R.; Daff, T. D.; Woo, T. K.; Huang, Y. Characterization of Zn-Containing Metal-Organic Frameworks by Solid-State ^{67}Zn NMR Spectroscopy and Computational Modeling. *Chem. Eur. J.* **2012**, *18*, 12251–12259, DOI: 10.1002/chem.201201563.

(49) Lucier, B. E. G.; Chen, S.; Huang, Y. Characterization of Metal–Organic Frameworks: Unlocking the Potential of Solid-State NMR. *Acc. Chem. Res.* **2018**, *51*, 319–330, DOI: 10.1021/acs.accounts.7b00357.

(50) Brozek, C. K.; Michaelis, V. K.; Ong, T.-C.; Bellarosa, L.; López, N.; Griffin, R. G.; Dincă, M. Dynamic DMF Binding in MOF-5 Enables the Formation of Metastable Cobalt-Substituted MOF-5 Analogues. *ACS Cent. Sci.* **2015**, *1*, 252–260, DOI: 10.1021/acscentsci.5b00247.

(51) MacKenzie, K. J. D.; Smith, M. E. Multinuclear Solid-State NMR of Inorganic Materials. In *Pergamon Materials Series, vol. 6*; Pergamon, Oxford, 2002; pp 3–727.

(52) Sarkisov, L.; Harrison, A. Computational Structure Characterisation Tools in Application to Ordered and Disordered Porous Materials. *Mol. Simul.* **2011**, *37*, 1248–1257, DOI: 10.1080/08927022.2011.592832.

(53) Mason, J. A.; Sumida, K.; Herm, Z. R.; Krishna, R.; Long, J. R. Evaluating Metal–Organic Frameworks for Post-Combustion Carbon Dioxide Capture via Temperature Swing Adsorption. *Energy Environ. Sci.* **2011**, *4*, 3030, DOI: 10.1039/c1ee01720a.

(54) An, J.; Rosi, N. L. Tuning MOF CO_2 Adsorption Properties via Cation Exchange. *J. Am. Chem. Soc.* **2010**, *132*, 5578–5579, DOI: 10.1021/ja1012992.

(55) Nandi, S.; Maity, R.; Chakraborty, D.; Ballav, H.; Vaidhyanathan, R. Preferential Adsorption of CO_2 in an Ultramicroporous MOF with Cavities Lined by Basic Groups and Open-Metal Sites. *Inorg. Chem.* **2018**, *57*, 5267–5272, DOI: 10.1021/acs.inorgchem.8b00304.

(56) Vaidhyanathan, R.; Iremonger, S. S.; Shimizu, G. K. H.; Boyd, P. G.; Alavi, S.; Woo, T. K. Competition and Cooperativity in Carbon Dioxide Sorption by Amine-Functionalized Metal-Organic Frameworks. *Angew. Chem. Int. Ed.* **2012**, *51*, 1826–1829, DOI: 10.1002/anie.201105109.

(57) Luebke, R.; Eubank, J. F.; Cairns, A. J.; Belmabkhout, Y.; Wojtas, L.; Eddaoudi, M. The Unique rht-MOF Platform, Ideal for Pinpointing the Functionalization and CO_2 Adsorption Relationship. *Chem. Commun.* **2012**, *48*, 1455–1457, DOI: 10.1039/C1CC15962C.

(58) Pal, A.; Chand, S.; Das, M. C. A Water-Stable Twofold Interpenetrating Microporous MOF for Selective CO_2 Adsorption and Separation. *Inorg. Chem.* **2017**, *56*, 13991–13997, DOI: 10.1021/acs.inorgchem.7b02136.

(59) Myers, A. L.; Prausnitz, J. M. Thermodynamics of Mixed-Gas Adsorption. *AIChE J.* **1965**, *11*, 121–127, DOI: 10.1002/aic.690110125.

(60) Lee, S.; Lee, J. H.; Kim, J. User-Friendly Graphical User Interface Software for Ideal Adsorbed Solution Theory Calculations. *Korean J. Chem. Eng.* **2018**, *35*, 214–221, DOI: 10.1007/s11814-017-0269-9.

(61) Shekhah, O.; Belmabkhout, Y.; Chen, Z.; Guillerm, V.; Cairns, A.; Adil, K.; Eddaoudi, M. Made-to-Order Metal-Organic Frameworks for Trace Carbon Dioxide Removal and Air Capture. *Nat. Commun.* **2014**, *5*, 4228, DOI: 10.1038/ncomms5228.

(62) Mohamed, M. H.; Elsaidi, S. K.; Pham, T.; Forrest, K. A.; Tudor, B.; Wojtas, L.; Space, B.; Zaworotko, M. J. Pillar Substitution Modulates CO_2 Affinity in "mmo" Topology Networks. *Chem. Commun.* **2013**, *49*, 9809–9811, DOI: 10.1039/c3cc44745f.

(63) Chen, K.-J.; Madden, D. G.; Pham, T.; Forrest, K. A.; Kumar, A.; Yang, Q.-Y.; Xue, W.; Space, B.; Perry, J. J.; Zhang, J.-P.; Chen, X.-M.; Zaworotko, M. J. Tuning Pore Size in Square-Lattice Coordination Networks for Size-Selective Sieving of CO_2. *Angew. Chem. Int. Ed.* **2016**, *55*, 10268–10272, DOI: 10.1002/anie.201603934.

(64) Chakraborty, A.; Roy, S.; Eswaramoorthy, M.; Maji, T. K. Flexible MOF–Aminoclay Nanocomposites Showing Tunable Stepwise/Gated Sorption for C_2H_2, CO_2 and Separation for CO_2/N_2 and CO_2/CH_4. *J. Mater. Chem. A* **2017**, *5*, 8423–8430, DOI: 10.1039/C6TA09886J.
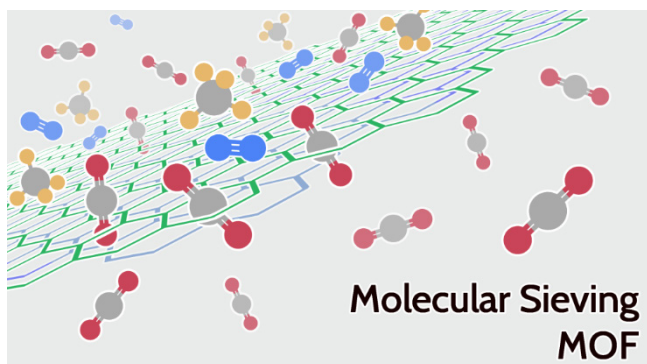
Tuneability of the pore aperture of MOFs for molecular size-based separations is an important factor for high analyte selectivity. We demonstrate the impressive impact that a small, sub-Å change has on the separation selectivity towards carbon dioxide in a MOF with pores able to exclude argon, nitrogen, and methane.